THE ASTROPHYSICAL JOURNAL, 472:14–24, 1996 November 20

ADDING LONG-WAVELENGTH MODES TO AN N-BODY SIMULATION

GIUSEPPE TORMEN[1]
Cambridge University, Institute of Astronomy, Madingley Road, Cambridge CB3 0HA, England;
bepi@ast.cam.ac.uk

AND

EDMUND BERTSCHINGER
Department of Physics, MIT, Cambridge, MA 02139; bertschinger@mit.edu
Received 1996 February 2; accepted 1996 June 6

ABSTRACT

We present a new method to add long-wavelength power to an evolved N-body simulation, making use of the Zeldovich approximation to change positions and velocities of particles. We describe the theoretical framework of our technique and apply it to a P^3M cosmological simulation performed on a cube of 100 Mpc on a side, obtaining a new "simulation" of 800 Mpc on a side. We study the effect of the power added by long waves by means of several statistics of the density and velocity field, and we suggest possible applications of our method to the study of the large-scale structure of the universe.

Subject headings: large-scale structure of universe — methods: numerical

1. INTRODUCTION

Computer simulations of large-scale structure play a fundamental role in cosmology by providing a better understanding of the many issues related to structure formation. The usual setup of an N-body simulation can be summarized as follows. One generates some initial conditions for the simulation by placing N^3 particles in a cubic box of side L. The recipe for assigning an initial position and velocity to each particle is usually the Zeldovich (1970) approximation. This approximation lets one distribute the particles in the box so that they trace some initial fluctuating density field with power spectrum $P(k)$. If the density fluctuations form a Gaussian random field, as is usually assumed, then $P(k)$ together with the evolution of the expansion scale factor specifies uniquely the cosmological model of the simulation. One then evolves this self-gravitating system by integrating numerically the trajectories of all the particles under their mutual gravitational attraction.

Periodic boundary conditions are commonly imposed on the box. Since a periodic function has a discrete Fourier transform, the periodic boundary conditions on the box imply a discrete sampling of $P(k)$: the only density fluctuations present in the evolution are those with wavelength $\lambda = 2\pi/k$ satisfying the usual periodicity requirement: $k^2 = (2\pi n_x/L)^2 + (2\pi n_y/L)^2 + (2\pi n_z/L)^2$, where n_x, n_y, and n_z are positive integers.

The two parameters L and N determine the dynamical resolution of the simulation. The box size L fixes the force resolution at large scales, since fluctuations on scales $\lambda > L$ are not included in the simulation and so are missed. It determines also the sampling resolution of the power spectrum $P(k)$: a larger L means a denser sampling of fluctuations at all scales, as $\Delta k \propto L^{-1}$. The particle number N^3 instead determines the force resolution at small scale because, for a given L, it fixes the minimum wavelength of the fluctuations present in the initial conditions, via the Nyquist relation: $k_{\max} = \pi N/L$, with $k = k_x, k_y, k_z$. Larger N values also mean more particles per object of interest, and therefore a better resolution in mass.

The ideal configuration is of course a large box size L and a large number of particles N^3. Unfortunately, even with the current supercomputer power, computer memory and CPU time impose severe limitations to the values of N^3 one can reasonably take. Given the maximum number N^3 of particles one can afford, the choice generally made is therefore to specialize the size L of the box to a specific purpose. For example, for a study of the general properties of a cosmological model, in which the identity and structure of single objects is of secondary importance compared to the overall large-scale structure and motions produced in the model, one will take a large box, i.e., with size $L \approx$ few $\times$ 100 Mpc, to the detriment of the small-scale resolution in force and in mass. On the other hand, when the interest is focused on the internal structure of the class of objects under investigation (e.g., galaxies or galaxy clusters), the box size L is taken much smaller, of the order of $\approx$few $\times$ 10 Mpc. In this case, there are two kinds of disadvantages. First, the missed fluctuations on scales larger than the box are still very important for the formation of structure. Second, since there are only three independent Fourier modes associated with density fluctuations of scale equal to the box size L, statistical fluctuations in the density and velocity fields are not negligible.

The missing power on large scales will cause a sort of *cosmic bias* (in the statistical sense of the term) because the number of high-density regions, the strength of the clustering, and the amplitude of the peculiar velocities will be systematically *lower* than in the ideal case of infinite N and L. The statistical fluctuations in different realizations of the same initial $P(k)$ on scale $\lambda \simeq L$ will instead introduce a *cosmic variance* in the simulation because the measures performed on the density and velocity field will fluctuate around their statistical mean value. Both effects can be dramatic if the volume L^3 is too small for the statistic one is considering, and they are particularly evident if one is interested in the peculiar velocity field, which receives important contributions from linear density fluctuations of very large scale. For example, in a standard cold dark matter (CDM)

[1] Present address: Max-Planck-Institut für Astrophysik, Karl-Schwarzschild-Strasse 1, 85740 Garching, Germany; bepi@mpa-garching.mpg.de.

universe with a dimensionless Hubble parameter $h = 0.5$, and a linear $P(k)$ normalized to an rms mass density fluctuation (in spheres of radius 8 h^{-1} Mpc) $\sigma_8 = 1$, the linear rms bulk velocity of a cube of side 100 Mpc is still well over 500 km s^{-1}. However, a simulation of 100 Mpc on a side will have zero bulk flow on the same scale because by definition the box is at rest. The missing power on scale $\lambda > 100$ Mpc is responsible for this cosmic bias. A good example of cosmic variance concerns the measure of the Hubble constant itself. This can assume quite different values locally because different patches of the universe are expected to expand at different *local* rates. Turner, Cen, & Ostriker (1992) have shown that, for a cold dark matter universe with *true* Hubble constant $h = 0.8$, the local Hubble constant measured out to 30 h^{-1} Mpc in regions comparable to the north Galactic cap has an estimated value $h = 0.5$–1.28 at the 95% confidence level.

The problems listed so far are well known in the literature of cosmological simulations of large-scale structure. However, attempts to solve them by inserting in a small-scale simulation the missing large-scale power have until now been limited to corrections applied to the mean values of the statistics [like $P(k)$ or the bulk velocity] (Couchman & Carlberg 1992; Strauss, Cen, & Ostriker 1993), or to the velocity field only (Strauss et al. 1995), but not individually to the velocity *and* density field. In this paper we propose a new method to cure these large-scale limitations. This method is applicable if the cosmic bias caused by the missing large-scale power is produced by density fluctuations that are still in the linear regime. The idea is then to use standard linear theory and the Zeldovich (1970) approximation to add to each individual particle of an *evolved* simulation of size L a random realization of the power coming from wavelengths larger than the original box size L. From this idea we named our method by the acronym MAP (mode adding procedure). The MAP corresponds to embedding the simulated cube in a much larger (and possibly infinite) one, therefore increasing the volume sampled and decreasing the cosmic bias and variance associated with it. Although there is virtually no upper limit to the scale of the added fluctuations, let us call $L_{\rm big}$ the scale of the largest fluctuations one reasonably wants to introduce.

A first straightforward application of this new method is the construction of different realizations of a very large scale simulation (e.g., 3000 Mpc on a side) from just one evolved medium scale (e.g., 200 Mpc) simulation. From this, one could extract artificial redshift surveys of size comparable to the real surveys completed or in program, e.g., the Las Campanas Redshift Survey (Landy et al. 1996), the ESO Slice Project (Vettolani et al. 1994), the Sloan Digital Sky Survey (Gunn & Weinberg 1994), and others. The resulting simulations would have at the same time a scale sufficient to address the issue, and enough resolution on small scale to identify properly galactic halos. The artificial surveys can be used to calibrate the different sources of uncertainties present in the real data (sparse sampling, redshift errors, etc.), to estimate the scientific impact expected from the new data, and to compare them with the predictions of different cosmological models, via a number of statistics. Other possible applications include the dynamical study of the role played in the structure formation process by linear density fluctuations on very large scale. Do they couple with nonlinear modes during time evolution? How do they trigger the formation of cosmic structure on all scales? How important are they when studying the velocity field or superclustering phenomena?

The paper is organized as follows. Section 2 is a description of our method. In § 2.1 we discuss the Fourier space manipulation required to apply our method to a simulation. Section 2.2 describes the corresponding steps performed in position space: a mode removing step and a mode adding step. In § 2.3 Lagrangian and Eulerian ways of implementing the technique are considered and discussed. In § 3 we apply the method to an N-body simulation and compare some statistics of the density and velocity field obtained from the MAP simulation with the same statistics applied to a real N-body simulation performed on large scale. Section 4 gives a summary of the results and presents some conclusions.

2. METHOD

2.1. *Fourier Space Manipulation*

The Fourier space of a periodic simulation can be thought as a cubic lattice. The sampling of the initial $P_\delta(k)$ is made on a regular cubic grid centered on $\boldsymbol{k} = \boldsymbol{0}$, ($|\boldsymbol{k}| \equiv 2\pi/\lambda$), with intergrid size $\Delta k = k_{\rm min} = (2\pi/L)$ and the extension in every direction determined by the number N^3 of particles used, via the Nyquist relation: $k_{\rm max} = \pi N/L$.

The diagram in Figure 1*a* shows the central region of this sampling. The dots correspond to the positions at which $P_\delta(k)$ is evaluated, and the regular grid divides the Fourier space in cubes of equal side Δk. Each cube is associated with a discrete Fourier component $\hat{\delta}_{\boldsymbol{k}}$ of the density fluctuation field $\delta(\boldsymbol{x})$: the intensity of density fluctuations of wavenumber $\boldsymbol{k}$ is the mean power per mode $\langle |\hat{\delta}_{\boldsymbol{k}}|^2 \rangle \approx P_\delta(k)(\Delta k)^3$. Including in the simulation density fluctuations on scales $\lambda > L$ corresponds to improving the sampling of $P_\delta(k)$ around $\boldsymbol{k} = \boldsymbol{0}$. Our scheme is thus a kind of mesh-refinement algorithm implemented in Fourier space.

Our approach is the following. First we remove, around $\boldsymbol{k} = \boldsymbol{0}$, the power associated with the Fourier modes of the original sampling. This means deleting the power of a number of cubes each of side $\Delta k = (2\pi/L)$ in the central region of Fourier space. Then we add back new power by filling the same region with a larger number of smaller cubes, each of side $\Delta k' = (2\pi/mL)$ (with m a positive integer). The power per mode of these new cubes is assigned with a random realization of the (Rayleigh distributed) linear power spectrum $P_\delta(k)$ at the corresponding positions; this ensures that the correct amount of power is added to the simulation. The procedure is sketched in Figure 1*b* for the case $m = 4$: a grid 4 times finer is substituted for the original one in Fourier space, out to an extension $r_k \equiv k/k_{\rm min} = 1$ in each direction. Subtracting a cubic region of extension r_k corresponds to removing $(2r_k + 1)^3$ cubes of side $2\pi/L$ from the Fourier space.

Our method adds long-wavelength power to a simulation at the end of time evolution. To ensure that the result is dynamically consistent, we must remove and add only power associated with fluctuations that are still in the linear regime. The linearity constraint may be interpreted in different ways. The most general requirement is that the root mean square density fluctuation associated with linear waves must be smaller than unity: $\sigma_\delta < 1$. Another straightforward characteristic of linear waves is that they evolve in agreement with the equations of linear theory. A third requirement is that linear waves should not couple dynami-

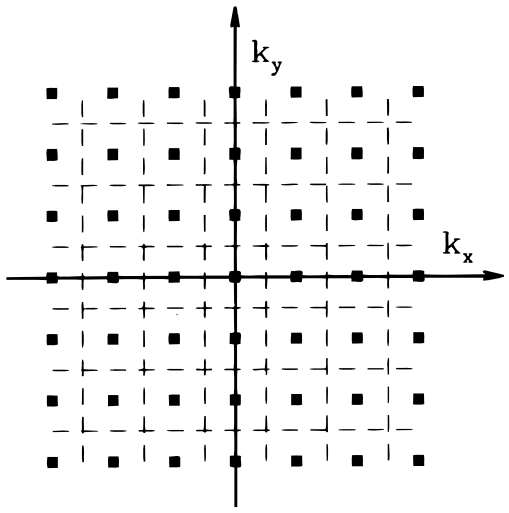

FIG. 1a

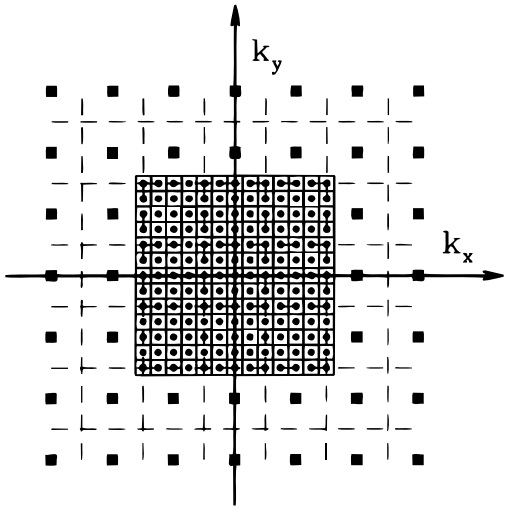

FIG. 1b

FIG. 1.—(*a*) Pictorial representation of the Fourier space for a periodic simulation on a cubic box with side L. The plot shows one plane of a three-dimensional distribution. Each small filled square corresponds to a position at which the power spectrum $P_\delta(k)$ is sampled by the initial conditions given to the simulation. The dashed grid divides the space in cubes of equal volume $(\Delta k)^3$, where $k = (2\pi/L)$, and each cube is associated with a mean power per mode $P_\delta(k)(\Delta k)^3$. (*b*) Pictorial representation of the Fourier space of a MAP simulation: adding power from wavelengths larger than the original L corresponds to placing a finer sampling of the power spectrum around $\boldsymbol{k} = \boldsymbol{0}$. See text for further discussion.

cally with any other wave. This issue has been explored by Jain & Bertschinger (1994), who find that for a cold dark matter spectrum of density perturbations mode coupling can transfer significant power to shorter waves from long wavelengths still nearly in the linear regime. We can monitor this by checking that the longest mode in our original box has linearly growing amplitude, but even this is not a rigorous limit because longer waves absent from the box might have caused the amplitude already to depart from linear growth. For now, we adopt the practical viewpoint of trying the method and testing later for effects of nonlinear coupling. We will discuss this issue further in the summary at the end of this paper.

Whichever linearity requirement we choose, this will put a limit on the region of Fourier space in which we can perform the power substitution. In the example of Figure 1, we manipulate the power in a cube of extension $r_k = 1$; depending on the simulation, we may extend the substituted region up to higher $\boldsymbol{k}$.

2.2. *The MAP idea: Mode Removing and Mode Adding*

To remove and add the power as described in § 2.1, we decided to use the displacement field and to perform the power manipulation by mean of the Zeldovich (1970) approximation. In this approximation, each fluid element moves along a straight line with a velocity extrapolated linearly from its initial velocity.

We will work in comoving coordinates with $\boldsymbol{q}_i$ and $\boldsymbol{x}_i$ being respectively the initial (Lagrangian) and final (Eulerian) position of the ith particle of the original simulation, $i = 1, 2, \ldots, N$. We will denote by $\boldsymbol{x}'$ the final particle positions after the mode removing step and $\boldsymbol{x}''$ the final positions after the mode adding step.

Before describing how we perform the mode substitution in practice, we will review briefly some relations between the density, velocity, and displacement fields that will be used later. The relation between the Eulerian and Lagrangian position of a fluid element at $\boldsymbol{x}$ is given by the displacement field $\boldsymbol{\psi}$: $\boldsymbol{x}(\boldsymbol{q}, t) = \boldsymbol{q} + \boldsymbol{\psi}(\boldsymbol{q}, t)$. By applying mass conservation and assuming that $\boldsymbol{x}(\boldsymbol{q})$ is one to one (no orbit mixing), we can write the exact relation

$$\delta(\boldsymbol{x}) = \left\| \frac{\partial \boldsymbol{x}}{\partial \boldsymbol{q}} \right\|^{-1} - 1 = -\nabla_q \cdot \boldsymbol{\psi}(\boldsymbol{q}) + O(\psi^2) \,. \tag{1}$$

Note that $\boldsymbol{\psi}$ is the full, nonlinear displacement. This relation is still mixing Lagrangian and Eulerian coordinates; however, in the linear approximation we may consider the displacement to be a function of $\boldsymbol{x}$ and write

$$\delta^{(1)}(\boldsymbol{x}) = -\nabla_x \cdot \boldsymbol{\psi}^{(1)}(\boldsymbol{x}) \,, \tag{2}$$

where now both $\delta^{(1)}(\boldsymbol{x})$ and $\boldsymbol{\psi}^{(1)}(\boldsymbol{x})$ are first-order quantities. We see how the time dependence of the linear displacement field is that of $\delta^{(1)}(\boldsymbol{x}, t)$, that is, considering only the growing mode $D_+(t)$: $\boldsymbol{\psi}^{(1)}(t) \propto D_+(t)$. Using this result and taking the time derivative of the mapping $\boldsymbol{q} \rightarrow \boldsymbol{x}(\boldsymbol{q})$, we obtain to first order the linear relation between the comoving peculiar velocity $\boldsymbol{v} \equiv d\boldsymbol{x}/dt$ and the displacement field at time t:

$$\boldsymbol{v}^{(1)}(\boldsymbol{x}) = H_0 f(\Omega) \boldsymbol{\psi}^{(1)}(\boldsymbol{x}) \,, \tag{3}$$

where $f(\Omega) = d\log D_+/d\log a \approx \Omega^{0.6}$. In particular, if $\Omega = 1$, the linear displacement field and the linear peculiar velocity field coincide if units of km s^{-1} are used. Zeldovich (1970) approximation is then written as

$$\boldsymbol{x}(\boldsymbol{q}) = \boldsymbol{q} + D_+(t)\boldsymbol{\psi}^{(1)}(\boldsymbol{q}) = \boldsymbol{q} + \frac{D_+(t)}{H_0 f(\Omega)} \boldsymbol{v}^{(1)}(\boldsymbol{q}) \,. \tag{4}$$

The steps we follow in practice are the following (all equations are meant at a given time t):

1. Starting with a simulation performed with N particles on a cubic volume L^3, we compute the comoving displacements as $\boldsymbol{\psi}_i = \boldsymbol{x}_i - \boldsymbol{q}_i$, $i = 1, \ldots, N$. We use these displacements to define a displacement field $\boldsymbol{\psi}$ on a regular grid in position space. This can be done in different ways, as we will see in the next subsection.

2. *Mode Removing.*—We decompose the displacement field into the contributions $\boldsymbol{\psi}^{\rm long}$, due to the modes that we

are going to subtract from the simulation, and $\psi^{\rm short}$ due to all the other modes: $\psi = \psi^{\rm long} + \psi^{\rm short}$. We subtract, the long-wavelength power from the simulation by interpolating $\psi^{\rm long}$ to the *Eulerian* position of each particle and subtracting it, changing in this way each particle's position. The velocities are changed in the same way, by taking advantage of the linear relation between them and the displacements in equation (3):

$$x_i' = x_i - \psi^{\rm long}(x_i) \; ; \quad v(x_i') = v(x_i) - H_0 f(\Omega)\psi^{\rm long}(x_i) \; ; \quad i = 1, 2, \ldots, N \; . \quad (5)$$

Another way to subtract the large-scale contribution to the velocities would be to decompose directly the velocity field as we did for the displacement, instead of using the linear relation between the two. We expect the two procedures to give the same result, as long as the basic assumption of removing only linear modes holds. Note that we did not subtract the displacements $\psi^{\rm long}$ at the q (Lagrangian) positions of the particles. If we did that, we would disrupt the nonlinear structures that formed during the evolution of the simulation and smear out the power on small scales. So far the change in positions does not make use of the Zeldovich approximation because the subtracted displacement is the actual one and not the initial one times the growth factor D_+. We are, however, assuming linear theory in the relation between the velocity and displacement fields, which is only approximate even for long waves.

3. *Mode Adding.*—We generate a new set of initial conditions consisting of random long-wavelength displacements $\psi_1^+, \ldots, \psi_N^+$ in a cube of side mL, by sampling randomly the power spectrum $P_\delta(k)$ only at those positions around $k = 0$ corresponding to the long-wavelength modes we are going to add. These displacements are then evolved linearly up to the present time, interpolated again to the *Eulerian* position of each particle, and added to the positions and velocities as prescribed by the Zeldovich approximation:

$$x_i'' = x_i' + D_+(t)\psi^+(x_i') \; ; \quad v(x_i'') = v(x_i') + D_+(t)H_0 f(\Omega)\psi^+(x_i') \; ; \quad i = 1, 2, \ldots, N \; . \quad (6)$$

The final result is a set of particle positions and velocities that now include the effect of density fluctuation waves as long as mL.

We stress the importance of adding the long-wave power by interpolating ψ^+ to the new positions x', not at the original positions x. In fact, in the MAP view the x values are just some *wrong* Eulerian positions at which the particles stand due to the missing large-scale power. Considering only the waves we subtract and add, we can identify x_i' with the Lagrangian position q. The correct way to apply the Zeldovich (1970) approximation is $x = q + D_+\psi^+(q)$, which indeed corresponds to equation (6). As a check, we also tried the alternative formulation: $x_i'' = x_i' + D_+(t)\psi^+(x_i)$. As expected, the results do not reproduce satisfactorily the linear long-wave power one is introducing.

2.3. *Lagrangian versus Eulerian Approach*

As sketched in § 2.2, we need to define a displacement field on a regular grid. This can be performed in two ways. Starting from a set of N displacements $\psi_1, \ldots, \psi_N$, we can assign each displacement ψ_i to its initial position q_i: $\psi_i \equiv \psi(q_i)$ and write

$$\psi_{\rm L}(q) = \frac{\sum_{i=1}^N \psi_i \delta_{\rm D}(q - q_i)}{\sum_{i=1}^N \delta_{\rm D}(q - q_i)} \; , \quad (7)$$

where $\delta_{\rm D}$ is a Dirac delta function. The subscript L stands for *Lagrangian* because the resulting displacement field is defined on a regular grid of initial positions.

Alternatively, we can assign every displacement ψ_i to the corresponding final position x_i: $\psi_i \equiv \psi(x_i)$ and interpolate such displacements onto a regular grid of final positions x_g by means of a suitable window function W; the resulting displacement field will be called *Eulerian* and indicated by a subscript E:

$$\psi_{\rm E}(x_g) = \frac{\sum_{i=1}^N \psi_i W(x_g, x_i)}{\sum_{i=1}^N W(x_g, x_i)} \; . \quad (8)$$

In subtracting the longest waves from the parent simulation, we used the Eulerian displacement field $\psi_{\rm E}(x)$, with a window function W corresponding to a triangular shaped cloud (TSC) interpolation on a regular cubic grid with 32^3 mesh points. The mode adding part was performed instead using the Lagrangian field $\psi_{\rm L}(x)$ because we assigned the displacements generated by the long waves to a grid of initial positions q as is usually done when generating standard initial conditions for a simulation. However, we do not expect the choice between $\psi_{\rm L}$ and $\psi_{\rm E}$ to be fundamental to the final result. In fact, the displacement fields we are considering are due only to long, linear waves; $(\psi_{\rm L} - \psi_{\rm E})$ at a given position is a second-order quantity.

In practice, the displacements employed by equations (5) and (6) are computed by interpolating the displacement field from the grid points to the Eulerian particle position:

$$\psi(x) = \frac{\sum_{x_g} \psi(x_g) W(x, x_g)}{\sum_{x_g} W(x, x_g)} \; , \quad (9)$$

where ψ may be either $\psi_{\rm L}$ or $\psi_{\rm E}$, and x is the particle position. The sum is extended over all the grid points x_g in the simulation. If $\psi_{\rm L}$ is used, the grid points x_g stand of course for the initial positions q_i, $i = 1, \ldots, N$.

3. APPLICATION TO A SIMULATION: MAP 8×144

As a first application of our technique, we will take a medium range, high-resolution N-body simulation, evolved originally in a periodic cube of side L, replicate it m^3 times in a larger cube, and add to it the missing power from the long wavelengths not sampled in the original cube, up to $\lambda = mL$. We use a P^3M N-body cosmological simulation of an Einstein–de Sitter cold dark matter universe, with a dimensionless Hubble constant $h = 0.5$, evolved in a cube of side $L = 100$ Mpc (Gelb & Bertschinger 1994). The simulation was run with 144^3 collisionless particles, each with mass $2.3 \times 10^{10} M_\odot$ and a Plummer softening radius of 65 kpc. We chose the output of the simulation corresponding to a linear normalization $\sigma_8 = 0.7$. We will refer to this simulation as P3M144. This simulation has high mass and force resolution and is particularly suited for studying the dynamics of cold dark matter halo formation and the small- to medium-scale structure. On the other hand, its size is too small to allow a study of the velocity field on large scales through statistics like the bulk flow or the velocity correlation tensor. We will compare statistics of the density and velocity field for P3M144, both before and after applying

the MAP, and for a reference N-body simulation evolved on a much larger scale. The latter, which we call P3M256, was run with identical cosmological parameters as P3M144, but it has 256^3 particles in a cube of side $L = 640$ Mpc and a Plummer softening radius of 160 kpc.

One way to verify the assumption of large-scale linearity for the fields in P3M144 is to measure the rms power associated with the long waves that are removed from and added back to it. The rms density fluctuation and displacement are defined directly in Fourier space respectively as

$$\sigma_\delta = \sqrt{\sum P_\delta(k)(\Delta k)^3} \quad \text{and} \quad \psi_{\rm rms} = \sqrt{\sum P_\delta(k)\,\frac{(\Delta k)^3}{k^2}}\,, \tag{10}$$

where the sums are extended over the modes under investigation. Referring to the picture of Fourier space in Figure 1, we tried the mode substitution on P3M144 in a cubic region of extension $r_k = 1$. This corresponds to removing the power associated with the 27 central cubes of side $\Delta k = (2\pi/100)$ Mpc^{-1} each. The displacement field associated with the removed region of Fourier space is what we called $\boldsymbol{\psi}^{\rm long}$ in equation (5). Its root mean square value computed from P3M144 as in equation (10) results in $\psi^{\rm long}_{\rm rms} = 7.1$ Mpc. The rms displacement due to all the wavelengths present in the simulation is $\psi_{\rm rms} = 11.2$ Mpc, showing how most of the displacement is due to the long waves present in the simulation. This is in agreement with what we said earlier about the peculiar velocities: both the velocity and displacement fields receive the biggest contribution from large-scale density fluctuations. This fact, however, does not invalidate our linear theory approximation because the long-wavelength displacement and velocities correspond to nearly uniform (bulk) motions for the particles, with no creation of nonlinear structures such as pancakes. This is confirmed also by the value of the rms density fluctuation due to the removed modes: $\sigma^{\rm long}_\delta = 0.55$ is less than one, as we would expect if the linear approximation applies. We will see if this is small enough when we compare with a larger simulation below.

We computed $P_\delta(k)$ from the simulation at different timesteps and plot in Figure 2*a* the growth rates of the lowest modes, normalized to the value of $P_\delta(k)$ at $a(t) = 0.1$. Figure 2*b* shows the analogous plot for P3M256, for comparison. Note that in this case the plot is normalized to a scale factor $a(t) = 0.2$, and the most evolved output of the simulation corresponds to $a(t) = 0.7$. From Figure 2 we deduce that all the modes of P3M144 up to $r_k(3)^{1/2}$ are approximately in the linear regime because their growth rate departs from the linear prediction by less than 20% even at the latest times. On the basis of these two tests, we conclude that $r_k = 1$ is a good choice for the region of Fourier space of P3M144, in which we will carry out our mode substitution.

We recall that the new sampling of the power spectrum around $\boldsymbol{k} = \boldsymbol{0}$ will have a resolution m times the initial one: $\Delta k' = \Delta k/m$, as shown in § 2.1. We estimated that $m = 8$, twice the resolution of the example in Figure 1*b*, is a reasonable choice. In terms of wavelength, this corresponds roughly to removing linear displacements generated by density fluctuations of scale $\lambda = 100$ Mpc and to adding back displacements associated with scales $\lambda \in [67,800]$ Mpc. However, since the geometry of Fourier space forced us to remove and add power in cubic regions, there are some shorter wavelengths removed and added as well, corresponding to the edges of the cube. Specifically, we remove modes up to a minimum $\lambda_{\rm min} = 58$ Mpc and add modes up to a minimum $\lambda_{\rm min} = 38$ Mpc. Considering a maximum fluctuation scale of 800 Mpc guarantees that we are including most of the power driving the velocity field for a standard cold dark matter model. In fact, a cube of side 800 Mpc has an rms bulk flow of roughly 150 km s^{-1} for $\sigma_8 = 1$, much lower than the bulk flow of the original box. Taking 8^3 replicas of the original simulation blows up the total number of particles to more than 1.5×10^9, too many for us to retain. We chose to keep a different random subsample of 32,000 particles from each of the 512 replicas of the original simulation, for a total of 16,384,000 particles over the (800 Mpc)^3 volume. We will refer to this simulation as MAP8 × 144.

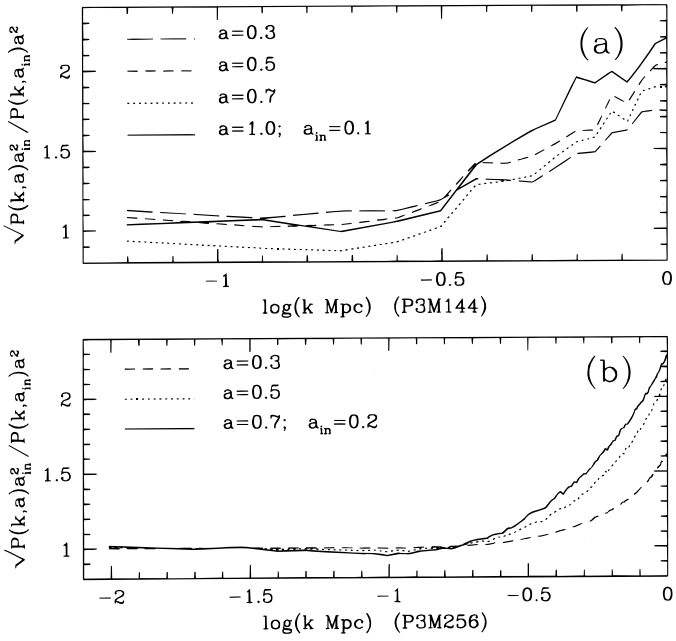

FIG. 2.—Rate of growth for the density fluctuation power spectra of (*a*) P3M144 and (*b*) P3M256. Growth is plotted as a function of k and is normalized to the growth predicted by linear theory. Deviations from the linear approximation show as departures of the curve from a unity value.

The rms displacement and density fluctuation due to the added modes and computed as in equation (10) are $\psi^+_{\rm rms} = 10.1$ Mpc and $\sigma^+_\delta = 0.63$ (we recall that the linear normalization for P3M144 is $\sigma_8 = 0.7$). We find, as expected, that the added power is larger than the power we subtracted from the simulation: $\psi^+_{\rm rms} > \psi^{\rm long}_{\rm rms}$ and $\sigma^+_\delta > \sigma^{\rm long}_\delta$. However, the extra power has been added in a way consistent with the power spectrum underlying the simulation and satisfying the requirements of the linear approximation.

The figures quoted for the rms density fluctuations associated with the removed and added modes might look high when compared to the normalization of the original simulation. In particular, one might wonder how the long waves can introduce an rms density contrast as large as $\sigma^+_\delta = 0.63$, if $\sigma_8 = 0.7$. The answer to this question is found in the different ways that were used to compute the density contrast. While $\sigma_8 = 0.7$ refers to a spherical top-hat filter, the figures associated with the long waves were computed with equation (10), which gives direct summations of the power of each mode with no filter function to smooth it.

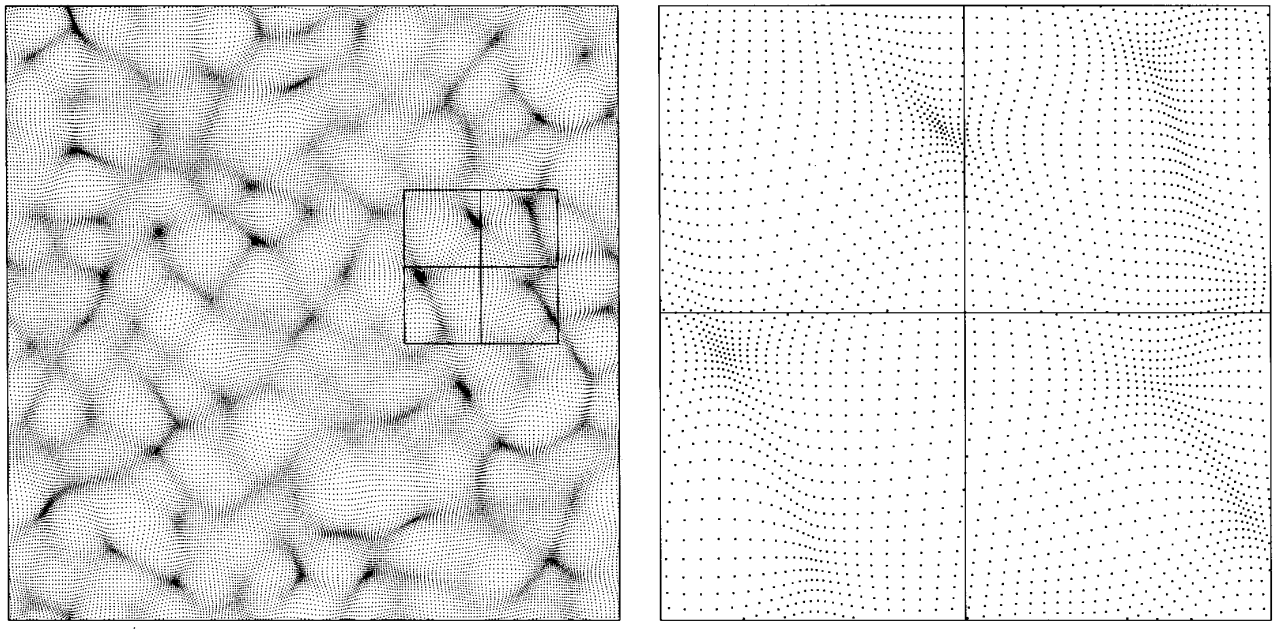

FIG. 3.—MAP applied to a Lagrangian slice of particles originally on a grid. We placed 200 × 200 test particles on a regular two-dimensional lattice of side 800 Mpc and displaced them by mean of the (three-dimensional) long-wave displacement field $\psi_+(x)$ described in the text. The field $\psi_+(x)$ has been generated using the same Fourier modes that will be added to P3M144, i.e., using only the power coming from scales between 800 Mpc and roughly 50 Mpc. *Left*: A projection of the entire slice; *right*: a blowup of 200 Mpc on a side taken from the left panel.

Equivalently, the filter function for the spherical top hat is sufficiently different from the filter function corresponding to the discrete mode distribution we are dealing with that a direct comparison of the two is not possible.

Throughout this section, we will compare the results and statistics from MAP8 × 144 with those from P3M144 and P3M256. We divide the analysis in two parts. The first part is dedicated to the study of the density field: we will show the effect of adding long wavelengths on both the morphology and the statistics. In the second part, we will study the velocity field.

3.1. *The Density Field*

To give a first visual impression of the effect of long waves on a distribution of matter, we applied the MAP to a two-dimensional sheet of regularly spaced particles. The result is shown in Figure 3: the modulation produced by the long waves is evident. The displacement field has moved the particles from their grid positions, creating density fluctuations on the required scales; the shortest fluctuations are of the order of 40 Mpc. In the most crowded regions, the particle trajectories are relatively close to shell crossing but have not yet reached it, as can be seen clearly in the right panel, which shows a blowup of the part of the slice enclosed by the square imprinted on top of the left panel. The magnified region, 200 Mpc on a side, is subdivided into four equal parts, each of which has the same size as P3M144. One can see how the effect of long waves on different replicas of the original simulation changes the global distribution of matter, modulating the preexisting structure in different ways on different copies.

Next we want to make sure that the small-scale, nonlinear clustering present in P3M144 is not changed or disrupted when we add the extra long-wavelength power. We tested this expectation by applying the MAP to a two-dimensional network of filaments, shown in Figure 4. After the action of the MAP, the network is still connected, i.e., the topology of the structure has not been modified by long-wave fluctuations. However, the filaments have been stretched here and compressed there, along all three dimensions, with different strength and effect in different places. We can measure how much "stretching" or "compression"

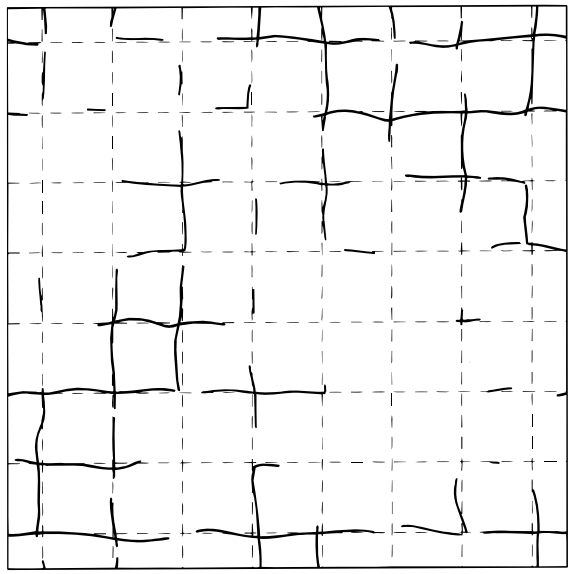

FIG. 4.—In a box of 800 Mpc on a side, particles were laid in order to mimic a two-dimensional network of one-dimensional structures. The particles were initially distributed in the x-y plane along $8 + 8$ filaments stretching across the box in both the x and y directions, as indicated by the dashed lines. The filaments have uniform density along their axis; each contains 5000 particles. The broken solid line shows how this network of particles has been modulated by the action of the long waves depicted in Fig. 3. The cut refers to a slice of thickness 20 Mpc. The sections of network apparently missing are just displaced along the line of sight (z-axis), enough to make them fell out of the slice shown here.

the long waves produced on the structure at different positions by looking at the derivative of the displacement field along the filaments. We chose randomly one of the 16 filaments shown in Figure 4 and computed the three components of the displacement field along it. These are shown in the first panel of Figure 5.

The displacements plotted in Figure 5 are continuous functions as expected, meaning that there is no "stripping" of two nearby particles due to the long waves. The total three-dimensional displacement of a particle is shown in the second panel. Its derivative tells us how much two initially close particles can be taken apart by the long waves. The steepest part of the function is blown up in the third panel. The derivative on the slope between $x = 500$ Mpc and $x = 520$ Mpc is approximately constant and has a value $ds/dx_0 \approx 0.5$. If we take this as a figure representative of the whole displacement field, it tells us that particles originally in a structure of size R will be taken apart at most by an amount equal to $R/2$, that is, half the size of the structure. Hence, the identity of, e.g., dark matter halos is preserved by the MAP if the mean interhalo separation is greater than the size of each individual halo. As this is usually the case, we do not expect the small structures of the halo to be disturbed appreciably by the action of the long linear waves of the MAP, although the final word on this issue can be given only by direct analysis of the halos through some group finding algorithm, which we have not yet done.

In Figure 6 we compare MAP8 × 144 and P3M256 by showing slices of 640 × 640 × 10 Mpc^3. The linear power spectrum normalization is $\sigma_8 = 0.7$ for all slices. In this figure, we sampled the particles of the three simulations so that the number of particles shown in each slice is approximately equal. Figure 6*a* shows a slice from the original P3M144, replicated over such a volume, prior to any mode substitution; the cut shows regions with structure as large as the whole original simulation P3M144, and the periodicity over 100 Mpc is evident. Figure 6*b* shows the same Eulerian slice after we performed the mode substitution. In Figure 6*b* most of the periodicity has been disrupted: the long waves have stretched here and compressed there the original pattern of clustering and voids, resulting in a more varied structure. New patterns have developed with a characteristic scale much larger than the original box size. Figure 6*c* shows a slice from the P3M256 N-body simulation. It is relatively easy for the eye to see the richer range in patterns of this true simulation when compared to Figure 6*b*. Such a comparison shows the residual periodicity of MAP8 × 144, in the form of cell-like structure of about the size of the original simulation, P3M144. Cells of similar size appear also in Figure 6*c*, but they are less evident due to their more irregular distribution. Although the figures give an idea of the performance of the MAP on large scales, they are also slightly misleading in that they do not show how much better MAP8 × 144 actually is on small scales owing to its better resolution when compared to P3M256. This can be shown only by specific tests, like the ones we are going to present in the next sections. On the whole, the largest structures which can be identified in Figures 6*b* and 6*c* have roughly the same size, of the order of about 150 Mpc. The relatively emptier regions seen in Figure 6*b*, in comparison with Figure 6*c*, are due to the sparse sampling we had to apply to P3M144 (roughly one particle in 90) in order to reduce the total number of particles in the (800 Mpc)^3 box to 16 × 10^6.

TABLE 1

DENSITY AND VELOCITY MOMENTS

Parameter	P3M144	MAP8 × 144	P3M256
$\langle\delta^2\rangle^{1/2}$	1.96	1.94	2.00
$\langle\|v\|\rangle$(km s^{-1}).....	655	722	699
$\langle v^2\rangle^{1/2}$ (km s^{-1}).....	768	827	804

In Figure 7 we plot the logarithm of the one-point density fluctuation distribution function $f(\delta)$ obtained by computing the density field on a regular lattice with 5 Mpc spacing using the TSC interpolation scheme. We also computed the rms density fluctuation for our various simulations; the values obtained are listed on the first row of Table 1. We see that MAP8 × 144 has a larger number of grid points with no particles and a longer tail of high overdensities. The abundance of empty grid points is due to the sampling problem noticed already in Figure 6*b*. In order to produce MAP8 × 144, we took only 32,000 particles from each copy of P3M144. This corresponds to an average of 32 particles contributing to the density value of each grid point; such a number is evidently too low to allow a good sampling of very underdense regions, which turn out completely empty. This does not happen for P3M144, in which the average number of particles contributing to a grid point is about 3000. As for P3M256, the figure shows that 64 particles per grid point seem enough for a good sampling, but this is probably due to the larger particle mass of this simulation.

Figure 8 shows $P_\delta(k)$ for P3M144, both before and after removing the long waves, as well as $P_\delta(k)$ for MAP8 × 144 and P3M256. The spectra have been computed using a 512^3 regular grid (128^3 for P3M144 after the mode removing); they include both a deconvolution from the interpolating scheme and a shot noise subtraction. The different starting

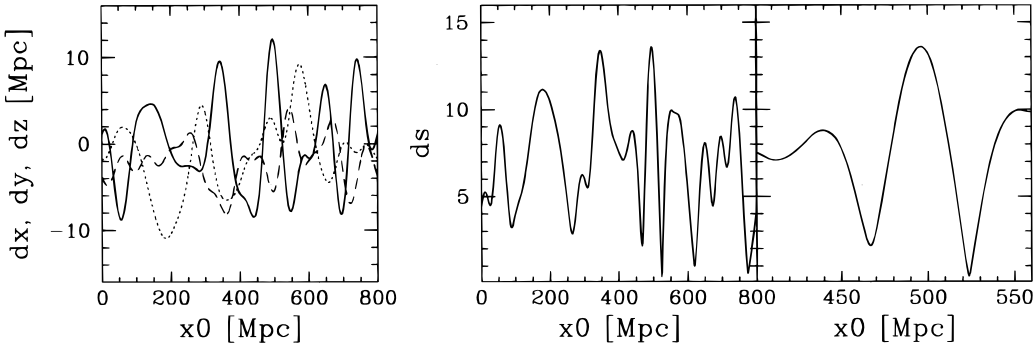

FIG. 5.—Displacement exerted by the MAP (in Mpc) on one of the filaments of Fig. 4. *Left*: Three components of the displacement field vs. the coordinate along the filament. *Middle*: Amplitude of the total displacement along the filament. *Right*: blowup of the steepest part of the middle panel.

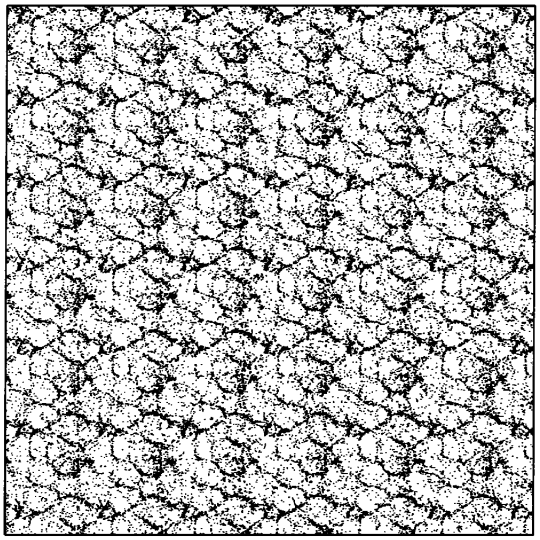

FIG. 6*a*

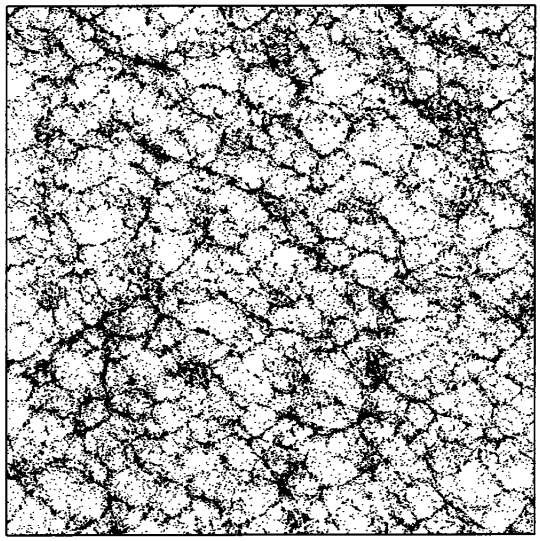

FIG. 6*b*

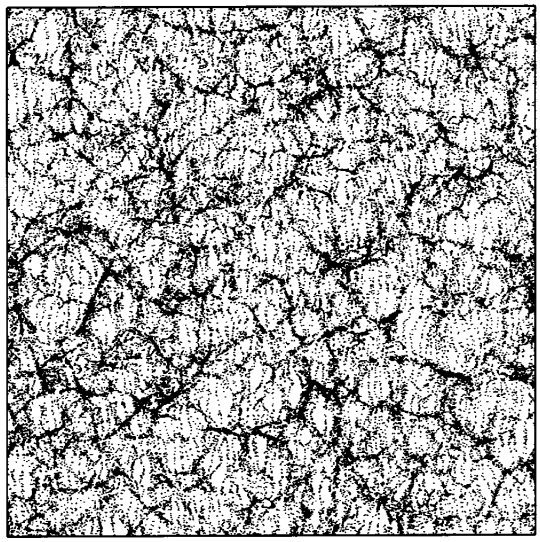

FIG. 6*c*

FIG. 6.—Eulerian slice taken from (*a*) P3M144, (*b*) MAP8 × 144, and (*c*) P3M256. Each slice is 640 × 640 × 10 Mpc^3. Only subsamples of particles from P3M144 are replicated in (*a*); in (*b*), the same Eulerian slice in (*a*) is shown, after long waves have been added up to a scale of 800 Mpc. In (*c*), a comparable slice from the true *N*-body simulation P3M256 is shown, performed in a volume of 640 Mpc on a side. Note that since in (*c*) only one particle of every two from P3M256 is plotted, a pattern appears as if particles were aligned along chains. This is just due to the grid used in the initial conditions.

and ending point for the curves are a consequence of the different scales of the simulations.

If our assumption of linearity is correct, we should see in $P_\delta(k)$ the same change in power that we performed on the displacement field. In fact, we do see that the amplitude of the power spectrum after mode removing has decreased by a factor of about 40 in the first bin, corresponding to modes with $\Delta k/k_{\rm min} \in [0.5, 1.5]$. We note, however, that the power spectrum after mode removing seems to be slightly lower than the original one: defining $b^2(k) \equiv P_\delta(k)/P_\delta^-(k)$, where $P_\delta^-(k)$ is the power spectrum of P3M144 after the mode removing step, we found that $b(k) \approx 1.15$ for high k. This may be due to some mode coupling between small and large k, caused by the fact that some of the subtracted waves are not evolving in a sufficiently linear way. If this is the case, then our tolerance of $\sim 20\%$ departures from linearity shown in Figure 2 would not be enough to ensure accuracy to better than 15%. To test this possibility, one could apply the mode removing to a larger simulation, e.g., twice the linear size of P3M144, and see if the effect is still there. On the other hand, the fact that P3M256 also has a power spectrum amplitude that is little lower than that of P3M144 on small scales suggests that the explanation of these differences could be more complicated.

As a check of our method, we tried also to subtract from P3M144 a larger number of modes, corresponding to cubes of extension $r_k = 2$, 3, and 4 in Fourier space. We found that removing shorter and shorter waves from the displacement field does not correspond to removing the equivalent power from the density fluctuations because the linear relation between the displacement and density fluctuation field breaks down for small scales.

The spikes shown by the power spectrum of the MAP simulation at $\log k \in [-1, -0.6]$ are an artifact due to the

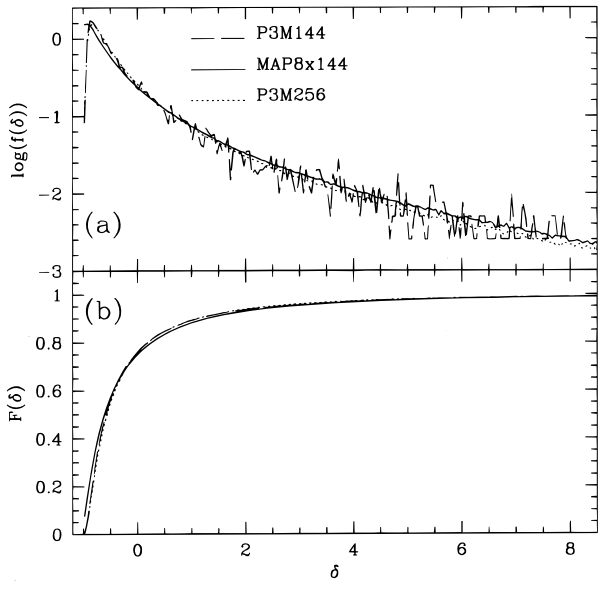

FIG. 7.—Density fluctuation distribution functions for P3M144 (*solid line*), MAP8 × 144 (*dot-dashed line*), and P3M256 (*long-dashed line*). Differential (*a*) and cumulative (*b*) distributions are plotted. In each case, the density has been calculated by interpolating the particle positions on a regular cubic lattice with intergrid spacing of 5 Mpc. A TSC interpolating scheme was used. See the text for discussion.

uneven sampling of power (as shown in Fig. 1*b*). This was not taken into account in the way $P_\delta(k)$ is evaluated numerically because the power summation is made in spherical shells with constant width $\Delta k = (2\pi/800)$ Mpc^{-1}. The effect shows up at values of k at which the old and new power sampling mix together, and it disappears at higher wavenumbers due to the higher number of modes present in each shell.

The global agreement of the power spectra of P3M144, MAP8 × 144, and P3M256 should imply an equally good agreement of the corresponding mass autocorrelation functions. Indeed, we found that this statistic differs by less than 35% (or 0.13 in logarithm) between the three simulations

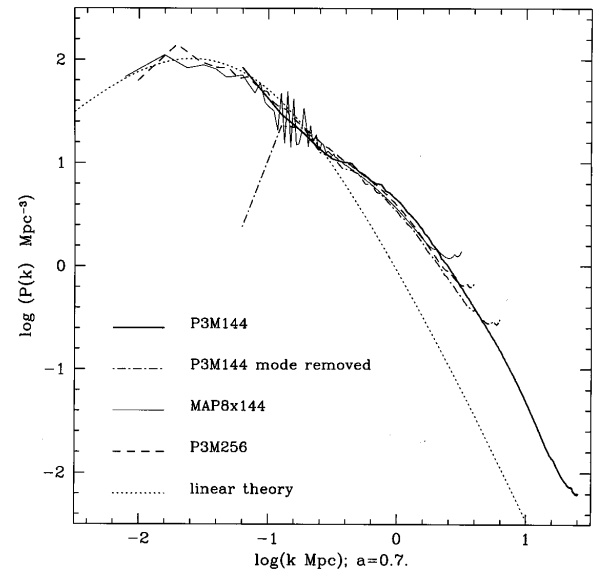

FIG. 8.—Density fluctuation power spectra for the three simulations. The plotted curves have been corrected for shot noise and have had the mass assignment scheme deconvolved.

over a range of pair separations not influenced by small-scale force softening or by border effects.

3.2. *The Velocity Field*

We would like to test the MAP performance on the velocity field in the same way as we tested the density field. Unlike the density, the velocity has the advantage of being defined (for single particles) without any smoothing, enabling us to study directly the distribution function of the raw particle velocities. In Figure 9 we plot the distribution function $f(v)$ of the velocity modulus for the three simulations. The gain in peculiar velocities due to the power associated with long waves is evident. Table 1 lists the first and second moment of the distributions for easy comparison. Besides increasing the peculiar velocities, long waves add coherence to the velocity field, so that the average velocity of a region of size 100 Mpc is roughly zero for the P3M144 simulation, but is of a few hundred km s^{-1} for the MAP simulation.

We would like to measure the velocity power spectrum $P_v(k)$ for the simulations. Unfortunately, this is not a very well defined quantity. In fact, in order to define a velocity field on a regular grid, one needs to take the ratio between the momentum and the density fields. If there are no particles in the neighborhood of a grid point, the density and the momentum will be zero there, and the velocity will be undetermined. Therefore, in order to define a velocity field at all grid points, one has to smooth the fields on a larger scale, so that some particles contribute to the density and momentum field of every grid point. However, in doing so information is lost on the velocity field at all scales smaller than the smoothing scale. Unlike the case of the density field, in which we could subtract the effect of the smoothing scheme by deconvolving $P_\delta(k)$ in Fourier space, here we deal with a ratio of convolved fields, which does not correspond to a simple multiplication in Fourier space. Hence, the deconvolution from the interpolating scheme is not possible

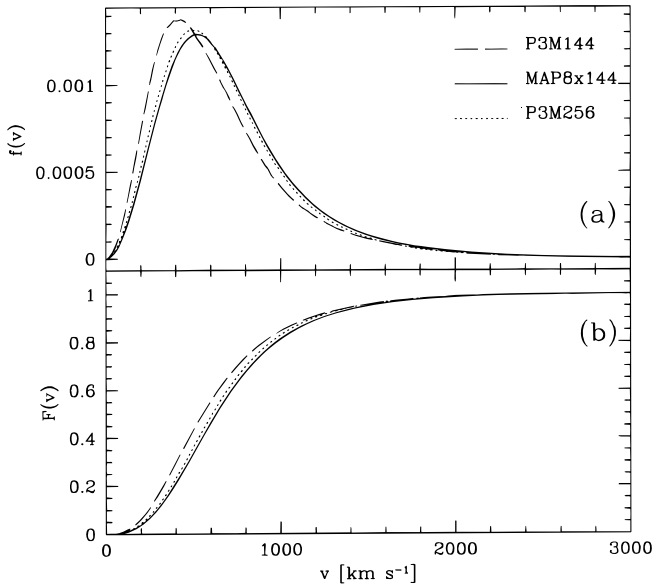

FIG. 9.—Differential and cumulative distributions for the magnitude of the peculiar velocities in P3M144, MAP8 × 144, and P3M256. Note the increasing of velocities with the box size. Velocities in MAP8 × 144 are even larger than those in P3M256, suggesting that nonnegligible contributions come from scales beyond 640 Mpc even for a standard CDM cosmological model.

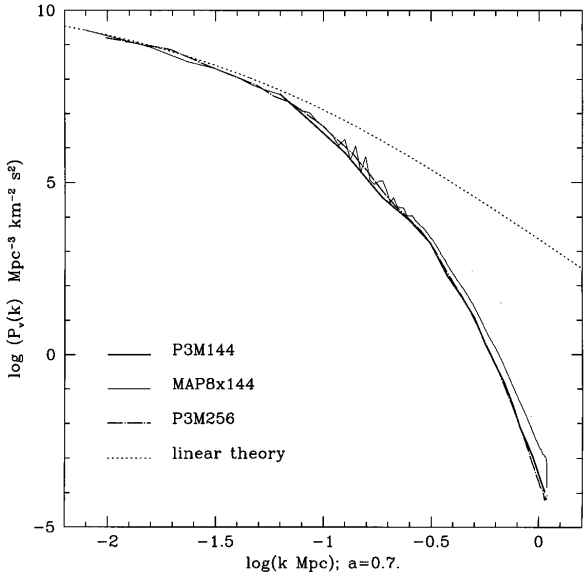

FIG. 10.—Power spectra for the longitudinal component of the velocity field, for the three simulations. A Gaussian smoothing filter of size 7 Mpc was applied to every field to define the velocity field also in underdense regions. The slight amplitude difference between MAP8 × 144 and P3M144 at high frequencies is not significative, as the velocity power spectrum is not well defined on small scales. Unlike $P_\delta(k)$, here no shot noise subtraction or window deconvolution has been applied.

for the velocity field. This sets a limit on the resolution of the velocity power spectrum at small scales.

In our case, to define the velocity fields of our simulations we evaluated the density and momentum density fields using TSC interpolation onto a 5 Mpc grid, followed by Gaussian smoothing of each with a kernel of size 7 Mpc before the ratio of fields is taken. Since in linear theory only the longitudinal component of the velocity field $\boldsymbol{v}_\parallel$ (defined by the irrotationality condition: $\nabla \times \boldsymbol{v}_\parallel = 0$) is related to the density fluctuation field $\delta(\boldsymbol{x})$, we considered only the power spectrum of $\boldsymbol{v}_\parallel$. Figure 10 compares $P_v(k)$ for P3M144, P3M256, and MAP8 × 144, superimposed on the linear prediction. The difference in amplitude between the latter and the power spectra of the three simulations at high wavenumbers is an effect of the filtering of the velocity field of the former.

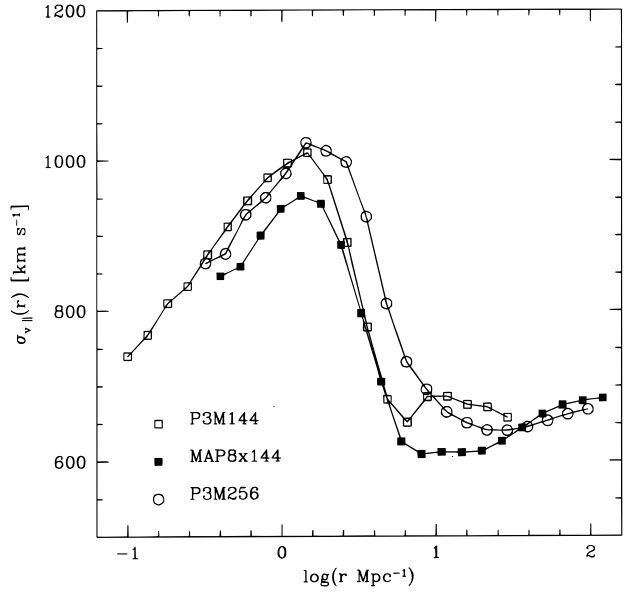

FIG. 11.—Parallel component of the pairwise velocity dispersion of the particles in the simulations.

We can see from the figure how $P_v(k)$ for the MAP simulation shows some amplitude difference over the spectra of both P3M144 and P3M256 on scales smaller than about 25 Mpc. This may again be related to the sampling problem discussed before, or to the invalidity of the linear approximation, but our current understanding of the effects of smoothing on the velocity field is too limited to allow a definite interpretation.

From the simulations, we also evaluated the pairwise velocity dispersion $\sigma_{v,12}$ as a function of pair separation. This is defined as the second central moment of the velocity field: given pairs of particles with velocities $\boldsymbol{v}_1$ and $\boldsymbol{v}_2$, separated by a distance r_{12}, the parallel component of the pairwise velocity dispersion is

$$\sigma_{v,12\parallel} = \langle [(\boldsymbol{v}_2 - \boldsymbol{v}_1) \cdot \hat{\boldsymbol{r}}_{12}]^2 \rangle^{1/2} , \tag{11}$$

where $\hat{\boldsymbol{r}}_{12} \equiv \boldsymbol{r}_{12}/|\boldsymbol{r}_{12}|$.

Since the value of $\sigma^2_{v,12\parallel}(r)$ is determined by the power associated with density fluctuations on scales $\lambda \lesssim 1/r$, the pairwise velocity dispersion is a suitable statistic to estimate the small-scale velocity power of a simulation. Figure 11 plots $\sigma_{v,12\parallel}$ for our three simulations; the three curves agree with each other to better than 10%. From this figure, our conclusion is that the MAP has not changed the velocity field significantly on small scales. Small differences between the curves are found also for P3M256 and may just reflect statistical fluctuations. The global agreement of this statistic contrasts somewhat with the different amplitudes of the velocity power spectrum between P3M144 and MAP8 × 144. This difference is not explained fully, but it could again be due to nonlinear effects in the MAP: the original simulation (L = 100 Mpc) might still be too small to guarantee a sufficient linear evolution for its fundamental modes, with $\lambda = L$. Mode coupling would then propagate to small scales any change in the large-scale power. Put another way, the pairwise velocity seems more robust than the velocity power spectrum in measuring the small-scale power.

4. SUMMARY AND CONCLUSIONS

We have proposed a new method to add to an N-body simulation the large-scale power associated with scales larger than the volume in which the simulation is performed. We made use of the Zeldovich approximation (Zeldovich 1970) to change each particle's position and velocity according to the extra power introduced. We tested the method using a simulation of standard cold dark matter, which we called P3M144. It had been evolved in a cube of 100 Mpc on a side by means of a P^{3}M code within 144^3 collisionless particles. We replicated the simulation to fill a cube of side 800 Mpc and added to it the power associated with fluctuations up to scales λ = 800 Mpc. We compared this enlarged simulation, named MAP8 × 144, with the original P3M144 simulation and with a larger simulation in a volume of 640 Mpc on a side called P3M256.

We showed both visually and by means of several statistics how the density and velocity field are modified by the addition of long waves: velocities are increased and structures are created with characteristic scales larger than the original box size. The rms velocity of a particle is $v_{\rm rms}$ = 768 km s^{-1} in P3M144, $v_{\rm rms}$ = 827 km s^{-1} for MAP8 × 144,

and $v_{\rm rms} = 804$ km s^{-1} for P3M256. The equivalent figures for the density field show that the MAP enhances slightly the preexisting clustering.

Our analysis of several statistics shows the effects of long waves in nonlinear simulations. The MAP procedure assumes that long and short waves evolve independently and that the former are describable by the Zeldovich approximation. However, our results suggest that there may be some transfer of power between long and short wavelengths in our simulations, for example, in the power spectra. If so, for accurate results our method may require stronger conditions than those met in our simulations. While a detailed study of this problem is beyond the scope of this paper, we can try to shed more light on this point by examining Figure 2*b*, which refers to the simulation P3M256, performed on a cube of 640 Mpc on a side.

We can identify three intervals of wavenumbers corresponding to different behaviors of the growth rates. The first interval corresponds to fluctuations with $\log (k \text{ Mpc}) \geq -0.8$ (i.e., $\lambda \leq 40$ Mpc); these grow faster than linear in all plotted outputs, and their growth becomes faster at later times, defining what is usually called the nonlinear regime. A second intermediate interval is approximately $-1.5 \leq \log (k \text{ Mpc}) \leq -0.8$ (corresponding to scales between 200 Mpc and 40 Mpc); fluctuations in this range grow slightly more slowly than the linear theory prediction, the effect becoming most visible at the latest time $a = 0.7$. Finally, fluctuations with wavenumber $\log (k \text{ Mpc}) \leq -1.5$ ($\lambda \gtrsim 200$ Mpc) maintain a strict linear growth (to within 1%) at all times. The analogous plot for P3M144 (shown in Fig. 2*a*) may suggest a similar behavior at least for $a = 0.7$, but unfortunately the growth rates are much more unstable due to the smaller size of the simulation, so that a definite interpretation is not possible.

The existence of these three regimes suggests that some coupling exists between the modes in the intermediate interval of wavenumbers and the modes in the nonlinear regime, with a transfer of power from the former to the latter. Transfer of power between long- and short-wavelength modes is consistent with the results of Jain & Bertschinger (1994): using second-order perturbative calculations for a CDM-like spectrum, they found that mode coupling cause a slight suppression of $P(k)$ at small k, and a significant enhancement at high k compared to the linear prediction, with the transition region occurring where the spectral slope is $n \lesssim -1$ (that is, $k \gtrsim 0.1$ Mpc^{-1}), respectively. If this interpretation is correct, then the size of P3M144 (100 Mpc on a side) is slightly too small to perform the mode substitution because the longest waves in the simulation are still weakly coupled with shorter wavelengths. Therefore, by subtracting the longest waves from P3M144 using our displacement field technique, we have also subtracted some power in the density field from small, nonlinear scales. The small-scale power, however, is not given back with the addition of long waves up to $L_{\rm big}$. In fact, the new large-scale power was not present during the simulation, but it is added randomly at the end of time evolution, and so it has no chance to enhance dynamically or suppress small-scale waves. Fortunately, even if some mode coupling affects the present example, it does not represent a limit of the method but just of the simulation we used to apply the MAP, so the conclusions we drew on the method are still valid. One obvious way to verify this hypothesis is to run the MAP starting with a simulation performed originally on a larger volume, for example, 200 Mpc on a side. In this case, we would expect to see no significant power transfer.

On a completely different issue, we would like to stress the point that our end product is not equivalent to a real simulation evolved from initial conditions on a comparable scale. In fact, outside the substituted region of Fourier space the MAP8 $\times$ 144 simulation samples high wavenumbers exactly like P3M144. That is, the density of Fourier modes there is not as high as in an N-body simulation actually performed on 800 Mpc on a side. Moreover, some small-scale periodicity may still be present in the final result, even if modulated by the large-scale waves.

The MAP can also be applied to any catalog of dark matter halos, or to any class of objects that can be defined in a simulation. In that case, however, one cannot trace back the Lagrangian position of the objects because they contain different particles and are defined during, or after, time evolution. What one does instead is to apply in equations (5) and (6) the displacement field obtained by the original particle distribution, which is parent to the halo catalog. That is, the displacement field of equations (7) and (8) is obtained from the particles.

Finally, the application of the MAP described in this paper concerns the study of very large scale density and velocity fields. However, other applications are possible, with focus on different aspects. In fact, the procedure that we have described here does not require at all the use of a box as large as the longest added wavelengths. Once the mode removing step is performed, one can interpolate the added displacement field to an arbitrary volume of the simulation. For example, in a study that does not require using a very large simulated volume, one can introduce the large-scale power in the original simulation without taking any replica. In such a case, all the particles of the original simulation may be used, to preserve the initial high definition and resolution.

We would like to thank Jim Frederic for providing the P3M256 simulation, and Sabino Matarrese and Simon White for useful comments and suggestions on an earlier version of the manuscript. We wish to thank the referee, Michael Strauss, for a helpful referee's report. Thanks are also given to the National Center for Supercomputing Applications, which provided our computer time. Financial support was provided by NSF grant AST 93-18185 and for G. T. also by the Italian MURST and by an EC-HCM fellowship.

REFERENCES

Couchman, M. M. P., & Carlberg, R. G. 1992, ApJ, 389, 453
Gelb, J., & Bertschinger, E. 1994, ApJ, 436, 467
Gunn, J. E., & Weinberg, D. H. 1994, in Wide-Field Spectroscopy and the Distant Universe, ed. S. J. Maddox & A. Aragon-Salamanca (Singapore: World Scientific), 3
Jain, B., & Bertschinger, E. 1994, ApJ, 431, 495
Landy, S. D., Schectman, S. A., Lin, H., Kirshner, R. P., Oemler, A. A., & Tucker, D. 1996, ApJ, 456, L1
Strauss, M. A., Cen, R., & Ostriker, J. P. 1993, ApJ, 408, 389
Strauss, M. A., Cen, R., Ostriker, J. P., Lauer, T. R., & Postman, M. 1995, ApJ, 444, 507
Turner, E. L., Cen, R., & Ostriker, J. P. 1992, AJ, 103, 1427
Vettolani, G., et al. 1994, in Wide-Field Spectroscopy and the Distant Universe, ed. S. J. Maddox & A. Aragon-Salamanca (Singapore: World Scientific), 115
Zeldovich, Ya. B. 1970, A&A, 5, 84